



Global Mapping of HCl on Mars by IRTF/iSHELL

S. Aoki¹ , S. Faggi^{2,3} , G. L. Villanueva² , G. Liuzzi⁴ , H. Sagawa⁵ , F. Daerden⁶ , S. Viscardi⁶ , S. Koyama⁷ , and A. C. Vandaele^{6,7}

¹ Department of Complexity Science and Engineering, Graduate School of Frontier Sciences, The University of Tokyo, 5-1-5 Kashiwanoha, Kashiwa, Chiba 277-8561, Japan; shohei.aoki@edu.k.u-tokyo.ac.jp

² NASA Goddard Space Flight Center, 8800 Greenbelt Road, Greenbelt, MD 20771, USA

³ American University, 4400 Massachusetts Avenue NW, Washington, DC 20016, USA

⁴ Scuola di Ingegneria, Università degli Studi della Basilicata, Via dell'Ateneo Lucano, 10, 85100 Potenza, Italy

⁵ Faculty of Science, Kyoto Sangyo University, Kamigamo Motoyama, Kita-ku, Kyoto 603-8555, Japan

⁶ Royal Belgian Institute for Space Aeronomy, 3 Avenue Circulaire, 1180 Brussels, Belgium

⁷ Tohoku University, 6-3, Aramaki Aza-Aoba, Sendai 980-8578, Japan

Received 2024 March 7; revised 2024 June 2; accepted 2024 June 13; published 2024 July 16

Abstract

Hydrogen chloride (HCl)—a key marker of the chlorine cycle on Mars—has been recently discovered in the Martian atmosphere by the ExoMars/TGO mission. In-orbit data indicate that this molecule appears in the atmosphere only in a limited time period and specifically in the southern summer season. A snapshot global mapping of HCl is indispensable to examine its sources and sinks, but such observations are not currently possible from any orbiters. Here, we present the first spatially resolved map of HCl obtained with the ground-based NASA InfraRed Telescope Facility. We find clear features of HCl, demonstrating that HCl is present close to the surface. HCl is detected in the equatorial region for the first time, revealing that HCl is widely distributed on Mars. However, the spatial distribution of HCl is not uniform, and it is enhanced in the southern polar region. Interestingly, this nonuniform spatial distribution of HCl column abundance is strikingly similar to that of water vapor column abundance. This highlights the important role of water vapor in the evolution of HCl through the atmosphere, as previously noted, and suggests its potential involvement in the atmospheric chlorine source processes.

Unified Astronomy Thesaurus concepts: [Planetary atmospheres \(1244\)](#)

1. Introduction

Hydrogen chloride (HCl) was recently discovered in the Martian atmosphere by the ExoMars Trace Gas Orbiter (TGO) mission (Korablev et al. 2021). HCl is the main reservoir of chlorine (Cl), marking the first detection of any Cl species in the atmosphere. On Martian soil, perchlorate salts ClO_4^- and chloride-bearing minerals Cl^- are widespread (e.g., Keller et al. 2006; Hecht et al. 2009), indicating the presence of hitherto unknown surface–atmosphere interaction on Mars. However, the Cl cycle remains unresolved, including the production and loss mechanisms of HCl.

Observations by ExoMars/TGO showed that the abundance of HCl in the atmosphere rapidly increases at the beginning of the southern summer when the atmosphere contains large amounts of floating dust ($L_s \sim 210^\circ$) and rapidly decreases at the end of the southern summer dusty period ($L_s \sim 330^\circ$). The highest abundance of HCl (~ 4 ppbv) is observed over the southern high latitudes in the middle of the local summer ($L_s \sim 270^\circ$), coinciding with water vapor release from the polar cap. This annual cycle has been observed to repeat in different Mars years (Aoki et al. 2021; Olsen et al. 2021). TGO measurements revealed that the vertical profiles of HCl and water vapor are strikingly similar (Aoki et al. 2021; Olsen et al. 2021), suggesting that the uptake by water ice clouds could play an important role (Kippenberg et al. 2019; Luginin et al. 2024). TGO measurements also showed that the isotope ratio

$^{37}\text{Cl}/^{35}\text{Cl}$ in the atmospheric HCl is consistent with the value on the surface measured by Curiosity and the terrestrial standard within the margin of error (Liuzzi et al. 2021; Trokhimovskiy et al. 2021).

Based on these results, the sources and sinks of HCl have been discussed in comparison with standard photochemistry. The most efficient predicted production pathway for HCl is the reaction between chlorine and hydroperoxyl radicals ($\text{Cl} + \text{HO}_2 \rightarrow \text{HCl} + \text{O}_2$). Hydroperoxyl is readily produced by the photolysis of water vapor; however, the mechanism by which Cl is released to the atmosphere remains unknown. One possibility is the release from floating dust, which contains chloride-bearing materials, through UV irradiation or electrostatic discharge (Krasnopolsky 2022; Wang et al. 2023). Considering only gas-phase chemistry, the photochemical lifetime of HCl in the lower atmosphere (below 15 km, where photolysis is the major sink) is estimated to exceed 90 sols (Aoki et al. 2021). However, this cannot explain the observed rapid decay of atmospheric HCl abundances around $L_s = 330^\circ$, suggesting the presence of an unknown strong sink.

The advantages of solar occultation measurements obtained by TGO are a high signal-to-noise ratio achieved thanks to the very bright Sun as a light source and the capability for vertical sounding. TGO measurements allow us to reveal a global picture of the seasonal cycle of HCl and its vertical distributions. However, there are some limitations. One of them is that solar occultation spectra cannot be obtained when aerosols along the line of sight obstruct the solar light. Thus, TGO measurements generally cannot investigate HCl abundances in the equatorial region and near the surface where aerosol abundances are high. As it cannot measure the HCl



Original content from this work may be used under the terms of the [Creative Commons Attribution 4.0 licence](#). Any further distribution of this work must maintain attribution to the author(s) and the title of the work, journal citation and DOI.

abundance close to the surface, determining the total atmospheric column abundance of HCl is not feasible. Another limitation is that the latitudes covered by the TGO measurements periodically change with solar longitude, preventing the capture of an instantaneous spatial distribution of HCl.

In this study, we present the first global map of HCl over the Mars disk, taken with the iSHELL, the high-resolution near-infrared echelle spectrometer (Rayner et al. 2022) installed at the NASA Infrared Telescope Facility (IRTF). Although there have been previous attempts to detect HCl from Earth, they provided only upper limits since they were performed outside the southern summer period: <0.3 ppb at $L_s = 77^\circ$ (Hartogh et al. 2010), <2.1 ppb at $L_s = 352^\circ$, <1.5 ppb at $L_s = 324^\circ$, and <0.6 ppb at $L_s = 12^\circ$ (Villanueva et al. 2013). On the contrary, our observations were performed on 2020 September 7 ($L_s = 273^\circ$ in Mars year (MY) 35) and 2020 November 1 ($L_s = 306^\circ$ in MY 35), i.e., during periods where TGO detected the HCl signatures. We employed the Lp1-custom band spectroscopy (upper wavelength $3.71 \mu\text{m}$) with a $15'' \times 0.375$ slit, which enabled us to acquire spectra with a resolving power of 90,000, covering a relatively wide spectral range from 2695 to 3024 cm^{-1} . In this spectral range, strong lines of CO_2 , H_2O , HDO , HCl , and CH_4 are available. The angular diameter of Mars is particularly large on both nights at about $20''$. The spatial resolution is limited by the seeing conditions of the terrestrial atmosphere at the time of the observations, which was around $0.5''$ for both dates. These observations allowed us to obtain a spatially resolved map of HCl and water vapor over the globe. We retrieved column density of HCl and water vapor from diffraction orders 151 ($2904\text{--}2928 \text{ cm}^{-1}$) and 141 ($2713\text{--}2736 \text{ cm}^{-1}$) of the iSHELL Lp1-custom setting, respectively. The measured spectra were compared with the synthetic spectra calculated by radiative transfer modeling.

2. Method

2.1. Observations

The observations of Mars by IRTF/iSHELL were carried out on 2020 September 7 and 2020 November 1. These dates correspond to $L_s = 273^\circ$ (the middle of the southern summer) and $L_s = 306^\circ$ (the end of the southern summer) in MY 35, respectively. These observations were performed during the middle and at the very end of the period in which the TGO measurements found an increase in HCl abundance. Table 1 provides an overview of the IRTF/iSHELL observations. On both dates, the Martian diameter was about $20''$, allowing detailed global mapping of HCl over the Mars disk. We employed the narrowest slit ($0.375''$) to achieve the highest spectral resolution (spectral resolving power, $R = 90,000$). The slit was aligned in the north–south direction. Given the slit length of $15''$, we scanned the whole Martian disk by moving the slit from north to south and across the east–west direction with a step of $2''$ (see Figure 1). For the first night, observations with 12 different slit positions were performed (6 different positions for each north/south hemisphere including the center position repeated twice). For the second night, observations with 10 different slit positions were performed. At each slit position, spectra of Mars and the sky (with a difference of $50''$) were acquired in positions A and B with the integration time of 60 s by nodding the telescope along the slit. Six ABBA cycles were performed for each slit position. The exact slit position was determined by comparing the measured flux with the

Table 1

Overview of the IRTF/iSHELL Observations Presented in this Study

Date (UT)	2020 September 7	2020 November 1
Mars years	35	35
Solar longitude ($^\circ$)	273	306
Mars diameter ($''$)	19, 9	20, 0
Seeing ($''$)	~ 0.5	~ 0.5
Doppler shift (km s^{-1})	-6	$+7$
Spectral range (cm^{-1})	2695–3024	
Spectral resolving power	90,000	
Slit length \times width ($''$)	15×0.375	
Slit positions	10 (5 for each hemisphere)	
Subsolar longitude ($^\circ$)	12.0E (at 12h UT)	261.9E (at 7h UT)
Sub-Earth longitude ($^\circ$)	42.76E (at 12h UT)	245.22E (at 7h UT)
Subsolar latitude ($^\circ$)	-25.41N (at 12h UT)	-20.18N (at 7h UT)
Sub-Earth latitude ($^\circ$)	-17.73N (at 12h UT)	-22.96N (at 7h UT)

theoretical surface albedo map (see Figure 1). Spectra of the Moon were also measured following the Mars observations to correct for systematic residuals in the removal of the telluric features. Flat-field frames were taken before and after the observations of Mars and the Moon for data calibration purposes. We used a custom Lp1 grating setting of iSHELL to cover $3.31\text{--}3.71 \mu\text{m}$ ($2695\text{--}3024 \text{ cm}^{-1}$), encompassing 17 diffraction orders (order 141–157). This setting allowed us to measure strong Martian lines of CO_2 , H_2O , HDO , HCl , and CH_4 . The Doppler shift between Mars and Earth was about $6\text{--}7 \text{ km s}^{-1}$.

2.2. Data Calibration

As described above, we nodded the telescope in the A and B positions for Mars, the Moon, and the sky following an $A_1B_1B_2A_2$ sequence. Sky frames are subtracted from Mars frames (i.e., $(A_1 + A_2) - (B_1 + B_2)$) to remove the telluric sky emissions and other instrumental features. The sky-removed Mars frames are averaged for each slit position, and flat-field is applied to the averaged Mars frames in order to remove the pixel-by-pixel detector variability and the global shape of the grating blaze function. Bad-pixel removal (e.g., due to cosmic rays) is also performed. After these standard data reduction steps, the stripe of each diffraction order is extracted from each frame. The extracted spectra are binned over three pixels ($\sim 0.5''$), which is comparable to the spatial resolution of the observations determined by the atmospheric seeing) along the spatial domain to increase the signal-to-noise ratio. The initial spectral calibration is performed using frames of the telluric sky emission for each slit position and detector row, followed by fine spectral calibration conducted with both telluric and Martian features.

2.3. Data Analysis

Since the targeted Martian HCl features are quite weak (less than a few percent over a few pixels), proper data analysis was conducted to eliminate systematics. Our analysis procedure of

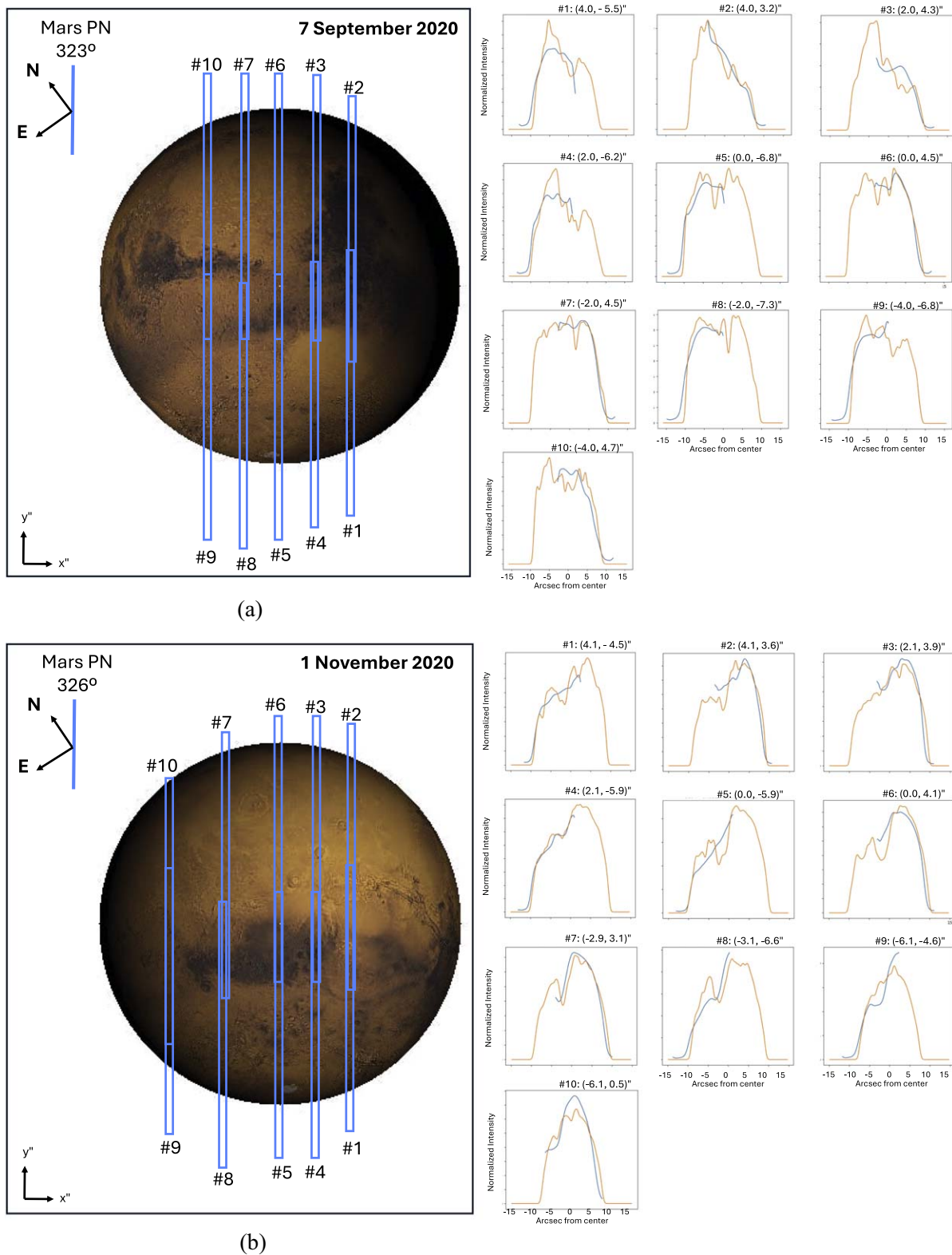


Figure 1. Mapping technique and slit positions for the Mars observations. During our observations the angular diameter of Mars was approximately $20''$. To map the whole planet disk, we set the iSHELL slit ($15'' \times 0.''375$) along the planet in the north–south direction, and we performed a scan across the east–west direction with a step size of $\sim 2''$, with a total number of ~ 10 slit positions. On the first date we also took a first initial center reference position, scan #1 and #2 in panel (a), providing a total of 12 slit positions for that observation. In Figures 1(a) and (b), we report the reconstructed hemispheric maps and the associated slit positions for the 2020 September 7 and November 1 observations, respectively. Slit positions were recovered by comparing the observed continuum fluxes at $3.4 \mu\text{m}$, extracted along the slit (blue profiles), with the modeled ones (orange profiles) generated from the albedo map included in the PSG (see PSG Handbook for more details; Villanueva et al. 2022). The position of the slit center, $(x, y)''$ for each mapping step is reported on top of each comparison.

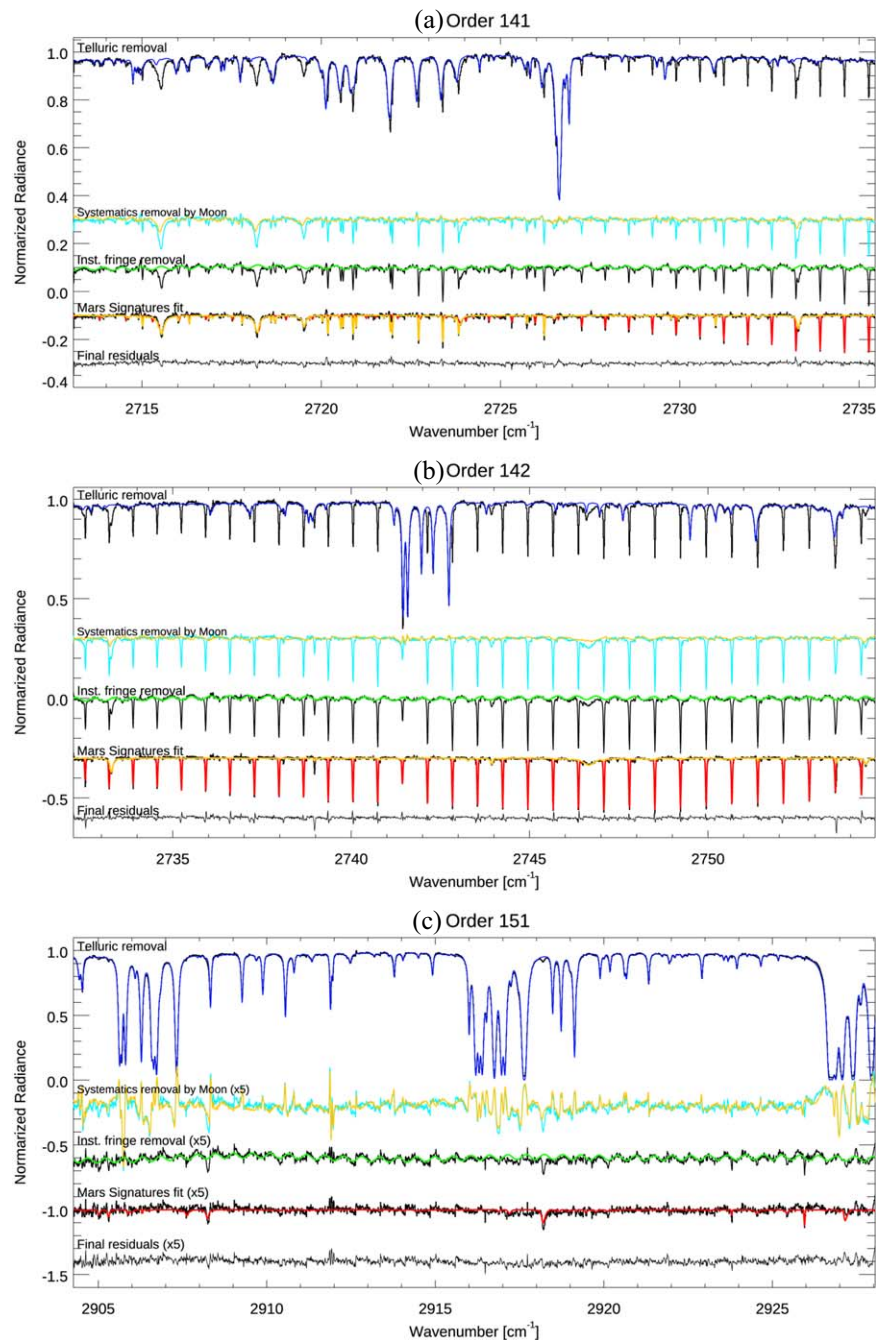


Figure 2. Examples of the data analysis of the spectrum at order 141 ((a), 2713–2736 cm^{-1}), order 142 ((b), 2732–2755 cm^{-1}), and order 151 ((c), 2904–2928 cm^{-1}). The black curves are measured IRTF/iSHELL data. The top curves show the removal of the telluric features (the blue curves are the synthetic spectra of the terrestrial atmosphere). The second top curves are the removal of the systematics by comparing Mars (light blue) and Moon (yellow) spectra. The middle curves show the removal of the instrumental features (“fringe”) as modeled by the green curves. The second bottom curves show the fitting of the Mars features (the red and yellow curves are the synthetic spectra of the Martian atmosphere with $\text{HCl}+\text{CO}_2$ and HDO , respectively), and the bottom curves are the final residuals.

the extracted spectra unfolds in three steps: (1) removal of the telluric features, (2) removal of the residual systematic features, and (3) retrieval of the Martian trace gases. The measured spectra contain features from the solar, telluric, and Martian atmospheres.

First, the telluric features are removed using synthetic spectra calculated by line-by-line radiative transfer (RT) modeling of the Earth’s atmosphere utilizing the Planetary Spectrum Generator (PSG; Villanueva et al. 2018, 2022). It

considers the atmosphere above the Maunakea Observatory (4.2 km altitude) to space across 53 atmospheric layers. Inputs for temperature, pressure, and composition are derived from NASA/MERRA-2 reanalysis data (Gelaro et al. 2017) corresponding to the measurement times, with observed zenith angles incorporated into the RT calculations. The best-fit synthetic telluric spectrum is determined for each pixel by scaling the vertical profile of water vapor and methane (see the top curves in Figure 2). A polynomial function is assumed for

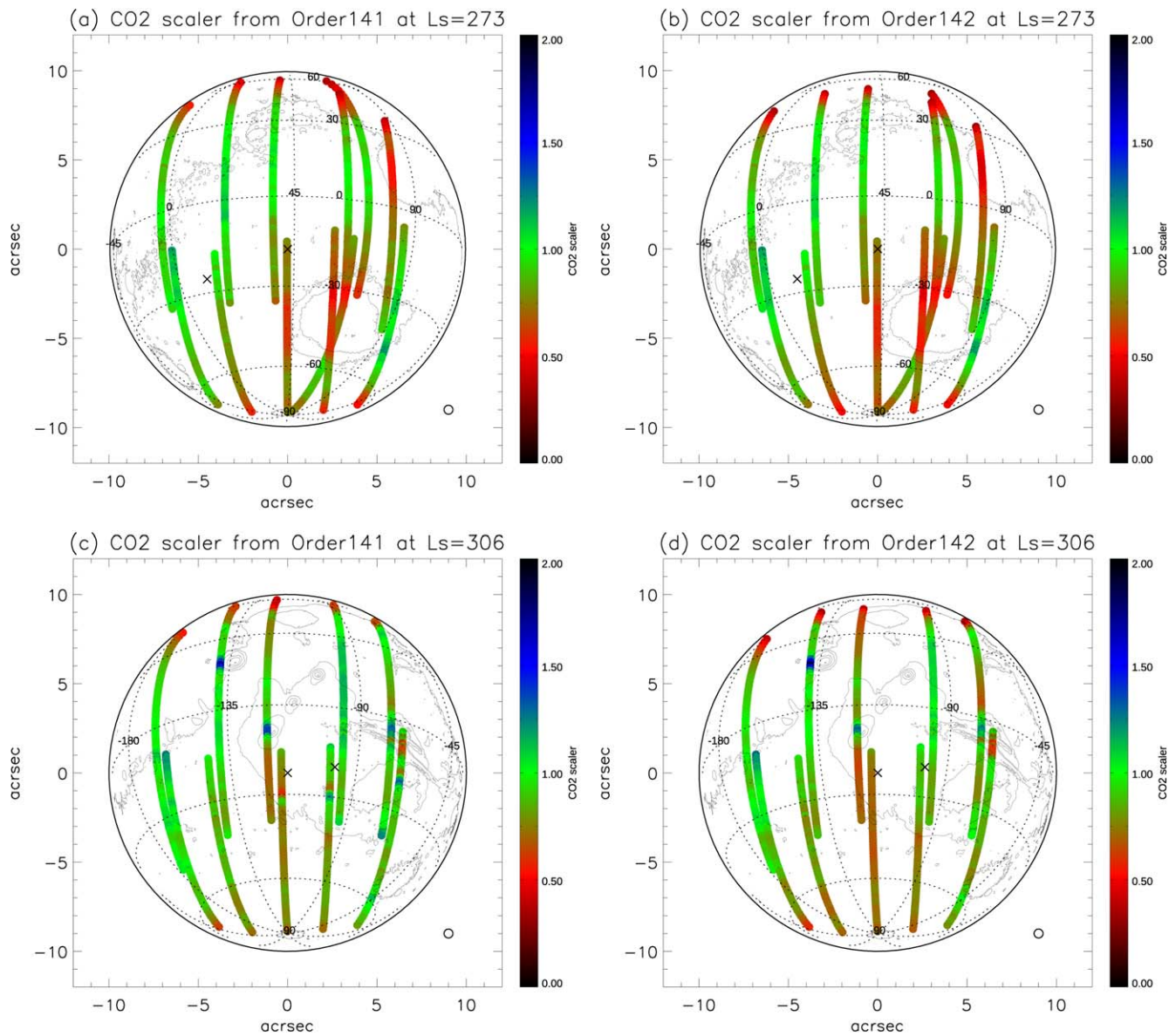


Figure 3. Global maps of CO₂ scaler retrieved from CO₂ lines at order 141 (a), (c) and order 142 (b), (d) from the observations at Ls = 273° (a), (b), and Ls = 306° (c), (d).

the global continuum, from which spectral points corresponding to features due to the Martian and solar atmospheres are excluded. This process applies to the Moon spectra as well.

Second, the difference between Mars and Moon residuals after removal of the terrestrial features is calculated (see the second curves from the top in Figure 2) to further mitigate residual systematics from instrumental and spectroscopic modeling. Still, a fringing feature emerges in the spectra, likely due to multiple reflections between two optical surfaces and the interference of the resulting wavefronts (Villanueva et al. 2013). Usually, the amplitude of this fringing feature is quite small ($\sim 1\%$ compared to the continuum flux) and can be removed by Lomb–Scargle periodogram analysis (Villanueva et al. 2013; see the third curves from the top in Figure 2).

Third, the abundances of Martian trace gases are determined. The forward RT calculations for the synthetic spectra of Mars atmosphere are also performed by PSG. It considers 49 atmospheric layers from the surface to 270 km. The Mars

Climate Database version 5.3 provides temperature and pressure profiles, while HCl and water volume mixing ratios are assumed uniform throughout the atmosphere. This assumption is reasonable for HCl as its signature is optically thin and most of the information comes from the lower atmospheric layers near the surface (i.e., column density). Effects of the multiple scattering due to aerosols are not taken into account in the calculation. The instrumental function of iSHELL is modeled as a Gaussian function with a spectral resolving power of 90,000. The fitting is individually performed for each spectrum taken at three different diffraction orders: order 141 ($2713\text{--}2736\text{ cm}^{-1}$; see Figure 2(a)), order 142 ($2732\text{--}2755\text{ cm}^{-1}$; see Figure 2(b)), and order 151 ($2904\text{--}2928\text{ cm}^{-1}$; see Figure 2(c)). The free parameters (i.e., retrieved quantity) of the fitting in each diffraction order are as follows: scalers for CO₂ and HDO profiles at the order 141 analysis, scaler for CO₂ at the order 142 analysis, and scalers for the HCl profile at the order 151 analysis. In addition to

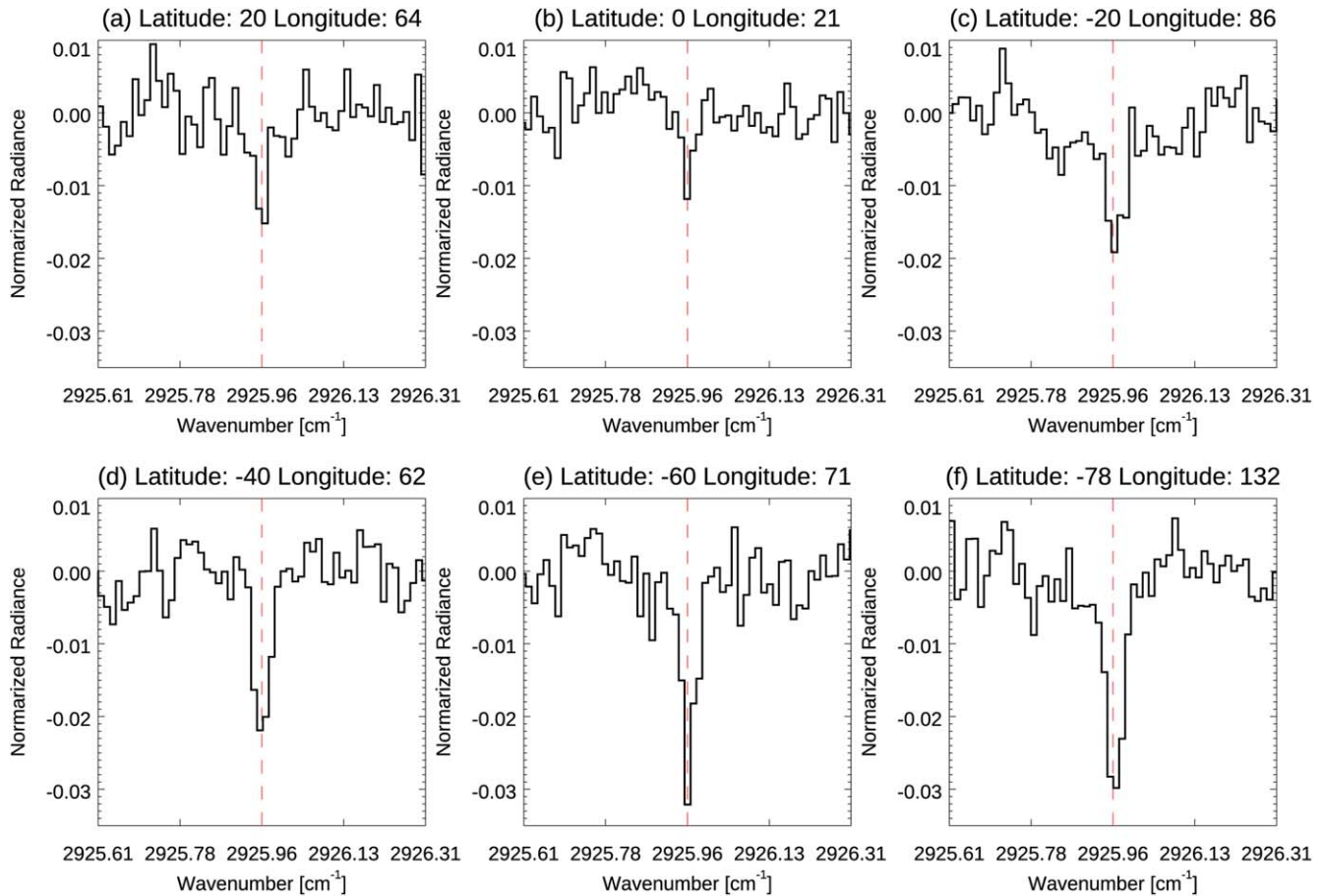


Figure 4. Examples of the extracted IRTF/iSHELL spectra focused at the spectral range between 2925.61 and 2926.31 cm^{-1} , which includes a strong HCl line at 2925.96 cm^{-1} . The expected wave number of the HCl line is illustrated as dashed vertical red lines. These spectra are measured at $L_s = 273^\circ$ at different latitudes around (a) 20°N, (b) 0°N, (c) 20°S, (d) 40°S, (e) 60°S, and (f) 78°S.

these, solar features are scaled for the analysis of all orders. The errors are evaluated based on the final residuals (the bottom black curves in Figure 2), which are the dominant source of the uncertainty in the retrieved values. The noise level is about 0.3% with respect to the continuum flux, which corresponds to about 0.5 ppb of HCl (1σ confidence, i.e., about 1.5 ppb for 3σ confidence).

As described above, radiative transfer calculations do not take into account the effects of aerosols. Instead, we use a “CO₂ scaler” (a factor adjusting the CO₂ column density from general circulation models) retrieved from order 142 to adjust for these effects. Given the ability of modern general circulation models to accurately predict CO₂ column density in the Martian atmosphere, the retrieved CO₂ scalars provide the effective air mass along the line of sight due to the presence of aerosols. Thus, dividing the retrieved HCl (or water vapor) volume mixing ratios by the CO₂ scalars yields the corrected abundances of HCl (or water vapor). Figure 3 shows the CO₂ scaler retrieved from order 142 (corrected for HCl and water volume mixing ratios) and that from order 141. The agreement between two orders underscores the reliability of our retrieval process.

The sensitive altitude of the column density retrieval of HCl with iSHELL data is 0–5 km above the surface except in southern high latitudes (greater than 70°S) where the sensitive

altitude is at 5–10 km above the surface due to longer air mass caused by the high solar zenith angle.

3. Results

3.1. Detection of HCl by IRTF/iSHELL

Figure 4 shows some examples of the observed iSHELL spectra taken at different latitudes (20°N, 0°N, 20°S, 40°S, 60°S, 78°S) within the spectral range between 2925.61 and 2926.31 cm^{-1} , which includes a strong HCl line. It is important to note that the actual data analysis encompasses the whole spectral range of order 151 (see Figure 2 and Section 2. Method for the details); however, Figure 4 specifically highlights a narrowed spectral range to focus on the strong HCl line at 2925 cm^{-1} . The Martian HCl features are distinctly visible at the expected wave number (the dashed red lines illustrated in Figure 4). This provides an independent confirmation of the HCl detection in the Martian atmosphere discovered by the TGO mission. Importantly, the Nadir observations by IRTF/iSHELL are sensitive to atmospheric layers close to the surface, which were not accessible with TGO. Therefore, the detections of HCl by IRTF/iSHELL reveal the presence of HCl down to the surface.

The amplitude of the detected HCl features ranges from 1% to 3% with respect to the continuum flux, surpassing the noise level of about 0.3%. As shown in Figure 4, the absorption

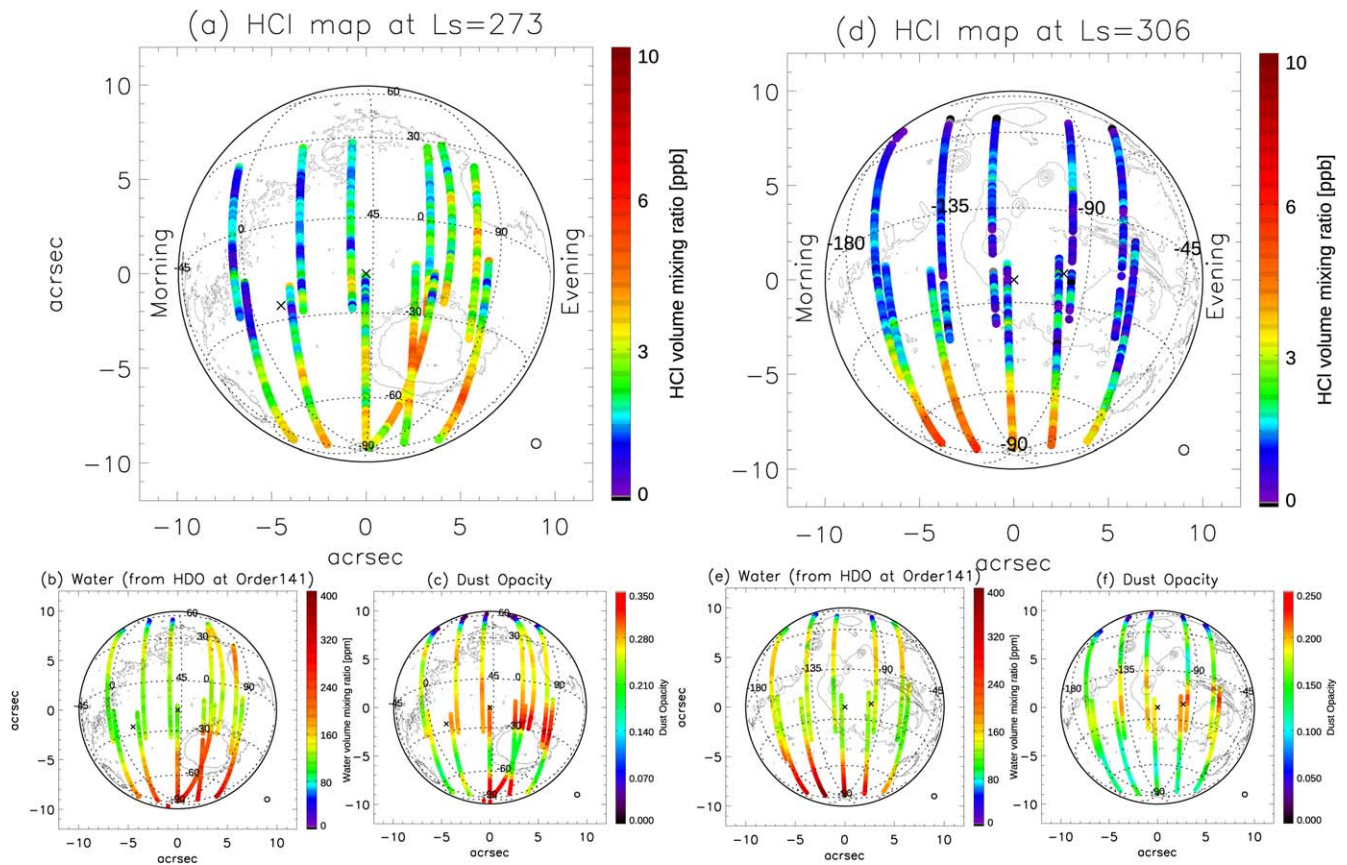


Figure 5. Global maps of the HCl volume mixing ratio (a), (d) and water vapor mixing ratio (b), (e) retrieved from the IRTF/iSHELL observations and dust opacity (c), (f) obtained from the database with MCS/MRO (Montabone et al. 2020) for $L_s = 273^\circ$ (a), (b), (c) and $L_s = 306^\circ$ (d), (e), (f) in MY 35. The cross symbols represent subobserver and subsolar points (the subobserver point is the center of the disk), and the black circles shown at the right bottom are the size of the spatial resolution limited by the atmospheric seeing at the time of the observations.

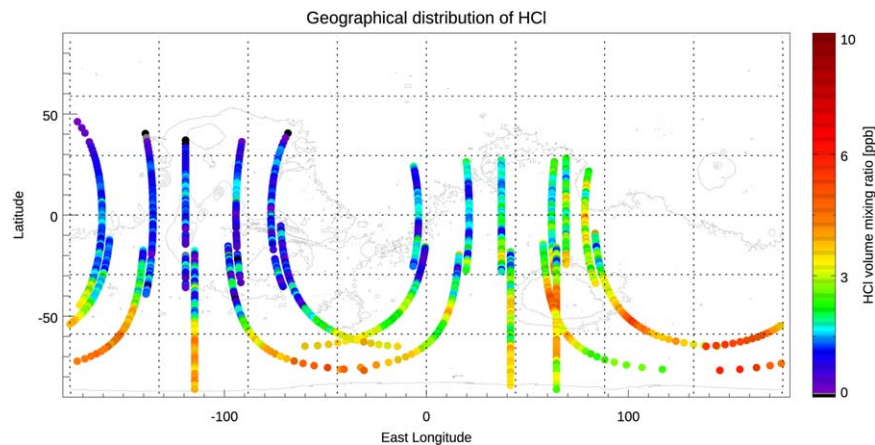


Figure 6. Geographical distribution of the HCl volume mixing ratio observed by IRTF/iSHELL. The results from the two different dates ($L_s = 273^\circ$, 306°) are shown in the same map.

depth of these HCl features becomes stronger toward the southern high latitudes (e.g., panels (d)–(f)). Moreover, despite a smaller absorption depth, the HCl features are also observed at lower latitudes (e.g., panels (a)–(c)). This marks the first detection of HCl in the equatorial region, an area where the TGO solar occultation measurements face challenges in conducting robust data analysis due to the presence of aerosols. This finding demonstrates that HCl is widely distributed over the Martian globe.

3.2. Global Map of HCl

Figures 5(a), (d) show the maps of HCl abundances obtained at $L_s = 273^\circ$ and $L_s = 306^\circ$, respectively, capturing different sides of the Martian globe. The retrieved HCl volume mixing ratios range from 0 to ~ 6 ppb. A remarkable observation is the nonuniform spatial distribution of HCl, with a significant enhancement in the southern high latitudes. TGO observations indicated a higher HCl volume mixing ratio in the middle

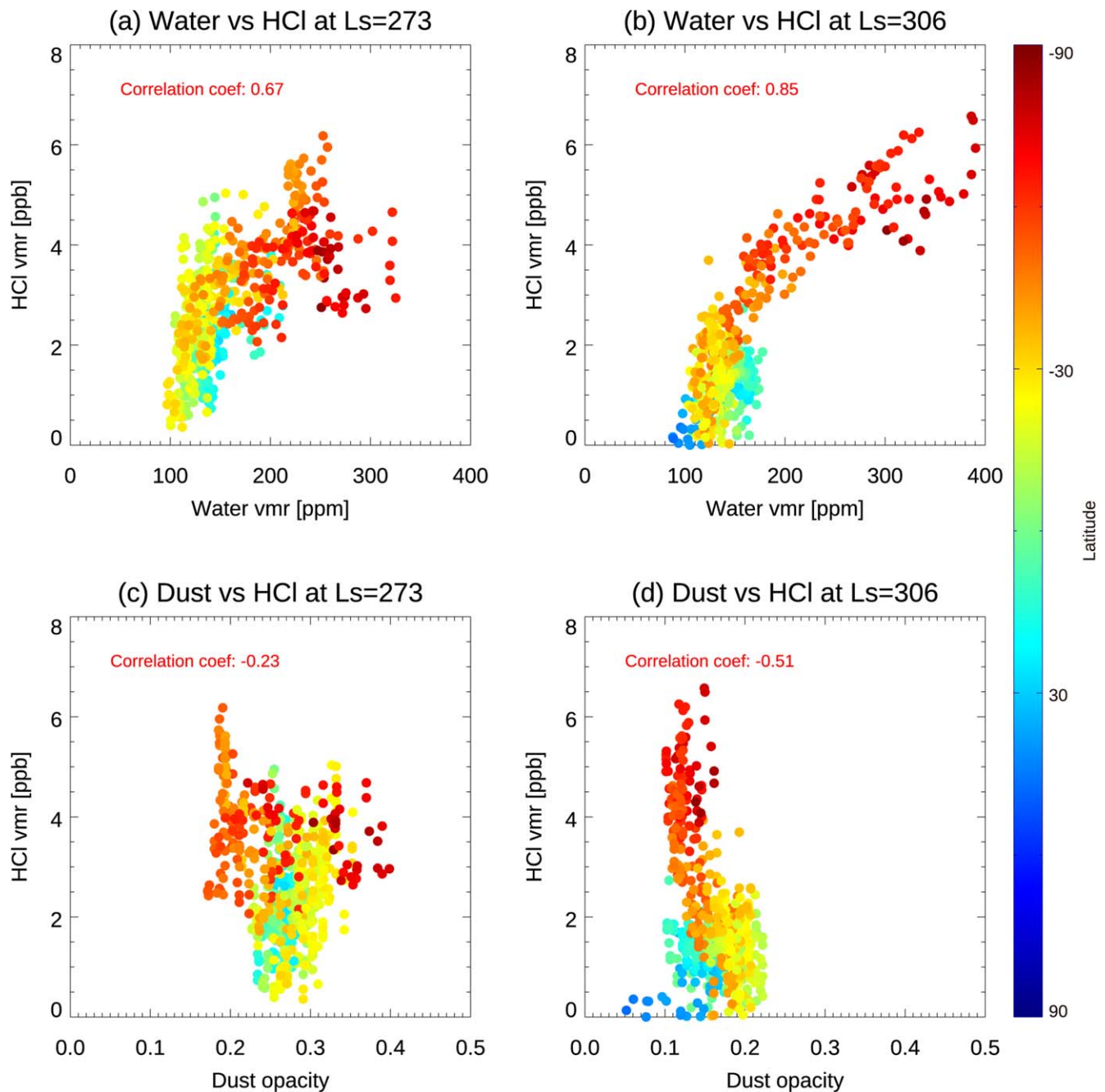


Figure 7. Comparison of HCl volume mixing ratio with water vapor volume mixing ratio (a), (b) and dust opacity (c), (d) for Ls = 273° (a), (c) and Ls = 306° (b), (d) obtained by IRTF/iSHELL observations. The bullets are color coded by the latitude at which the measurements were taken.

atmosphere (5–40 km) of the southern hemisphere compared to the northern hemisphere, albeit limited to middle latitudes (e.g., see Figure 2 in Aoki et al. 2021). This finding aligns with the instantaneous global maps obtained by IRTF/iSHELL. The retrieved volume mixing ratios of HCl by IRTF/iSHELL are consistent with those obtained by TGO.

In the global map of HCl obtained on the first night (at Ls = 273°), a higher HCl volume mixing ratio is observed toward the east, indicating an increase from the morning to the evening side. Conversely, in the HCl map from the second night (at Ls = 306°), higher HCl values are observed toward the west, signifying an increase on the morning side. This behavior suggests that the variation in the HCl volume mixing ratio is not controlled by a regular diurnal cycle. Moreover,

patchy, small spatial distributions of the HCl volume mixing ratio, exceeding the uncertainty of the HCl retrievals (~ 1.5 ppb for 3σ ; see Method section), suggest that HCl abundances are highly variable in space. The global and local spatial variability of HCl are not correlated with topography (see the geographical distribution of HCl shown in Figure 6).

3.3. Relationships with Water and Dust

Figures 5(b), (d) show the maps of the water vapor volume mixing ratio determined from the retrievals with the HDO lines in diffraction order 141 ($2713\text{--}2736\text{ cm}^{-1}$; see Figure 2), assuming that the D/H ratio in water vapor is uniformly 5 times larger than the terrestrial standard value. Daerden et al. (2022) show that the

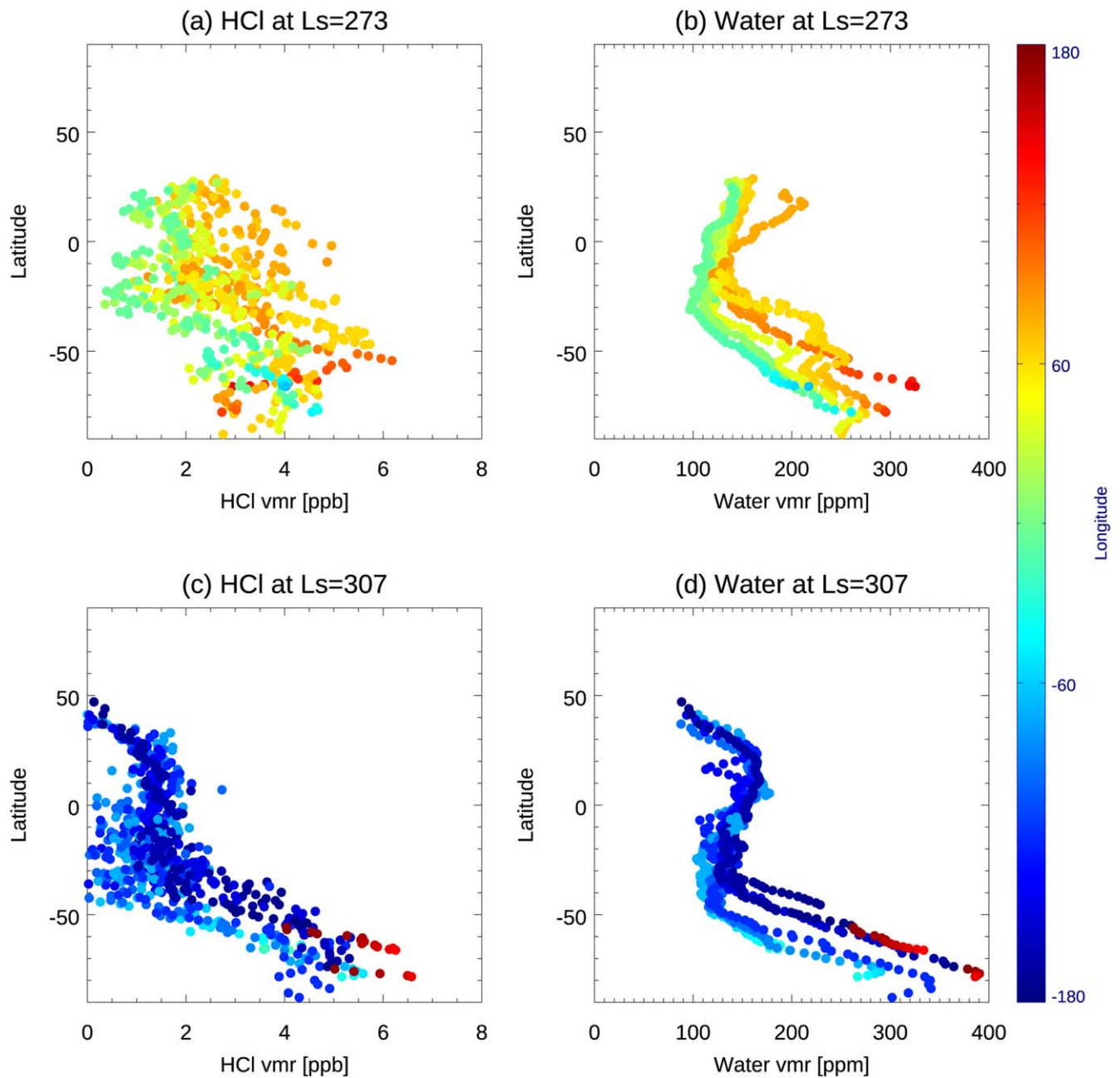


Figure 8. Latitudinal distributions of HCl volume mixing ratio and water vapor volume mixing ratio for $L_s = 273^\circ$ (a), (b) and $L_s = 306^\circ$ (c), (d) obtained by IRTF/iSHELL observations. The bullets are color coded by the longitude at which the measurements were taken.

simulated horizontal D/H distribution is highly uniform in this season. The resulting maps reveal a pronounced enhancement in water vapor at the high southern latitudes on both dates, attributable to the sublimation of seasonal polar ice composed of water ice during the local summer (e.g., Smith 2002). These water vapor abundances are consistent with previous studies (e.g., Smith 2002). Interestingly, the spatial distribution of water vapor is strikingly similar to that of HCl, encompassing global and local variations. Figures 7(a), (b) show the correlation between water vapor and HCl volume mixing ratios at $L_s = 273^\circ$ and $L_s = 306^\circ$, respectively, indicating a strong correlation (with correlation coefficients of 0.67 for $L_s = 273^\circ$ and 0.85 for $L_s = 306^\circ$). We also find that the correlation coefficients are larger at 30°S – 90°S (0.58 for $L_s = 273^\circ$ and 0.88 for $L_s = 306^\circ$) compared to those at other latitudes (0.40 for $L_s = 273^\circ$ and 0.34 for $L_s = 306^\circ$). This

strong correlation between HCl and water vapor volume mixing ratios is also clearly visible in their latitudinal distribution, as shown in Figure 8.

Figures 5(c), (f) display maps of the expected dust opacity for the locations and seasons corresponding to the IRTF/iSHELL measurements derived from a dust opacity database based on observations from the Mars Climate Sounder (MCS) on board NASA's Mars Reconnaissance Orbiter (MRO) (Montabone et al. 2020). These maps align reasonably well with the CO_2 scaler maps retrieved from diffraction orders 141 ($2713\text{--}2736\text{ cm}^{-1}$) and 142 ($2732\text{--}2755\text{ cm}^{-1}$), as depicted in Figure 3. Interestingly, in contrast to water vapor maps, the predicted global dust maps (Figures 5(c), (f)) do not resemble the HCl maps (Figures 5(a), (d)). Indeed, there is no observed correlation between dust opacity and the HCl volume mixing

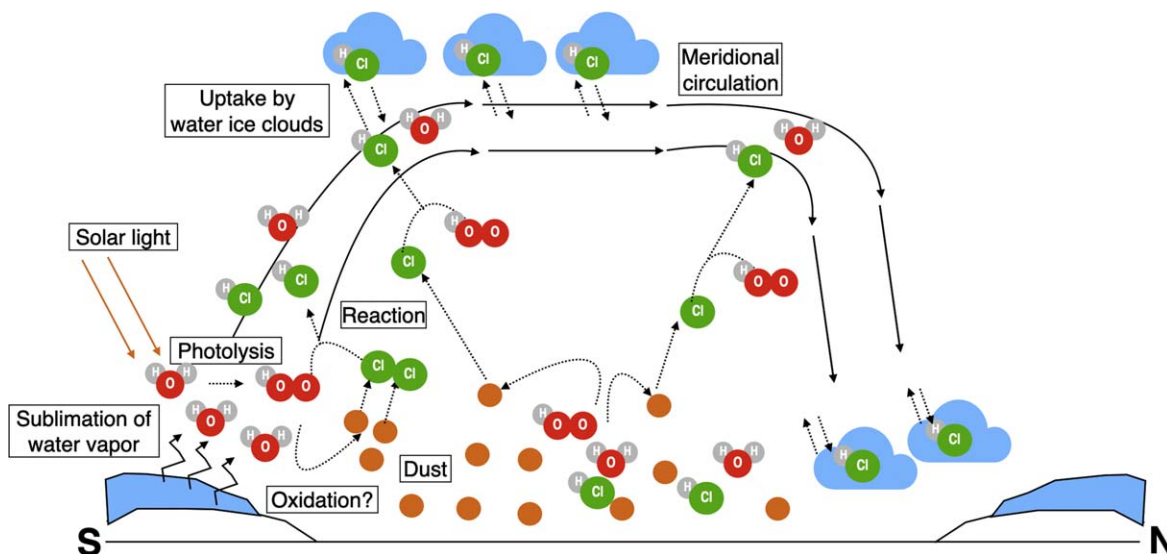


Figure 9. Potential processes of the HCl cycle proposed based on the solar occultation measurements by TGO global mapping by IRTF/iSHELL. Note that this diagram primarily focuses on the dusty season on Mars.

ratio on either date, as shown in Figures 7(c), (d) (with correlation coefficients of -0.23 and -0.51 for $L_s = 273^\circ$ and $L_s = 306^\circ$, respectively).

4. Discussion and Conclusion

This study reveals the presence of HCl in the equatorial regions, with observed instantaneous maps of the HCl volume mixing ratio showing higher values at southern high latitudes compared to lower latitudes. This trend contrasts with that of standard noncondensable gases. For instance, during the local summer, the latitudinal distribution of the CO volume mixing ratio decreases at summer high latitudes due to sublimation from the seasonal CO₂ polar cap (e.g., Bouche et al. 2021). This suggests that local HCl production and/or loss processes influence its spatial distribution. Figure 9 outlines potential processes that can consistently contribute to the observed HCl spatial variation.

The observed high abundances of HCl at southern high latitudes could indicate the significant role played by water vapor in the appearance and evolution of HCl. Released by the sublimation of the seasonal polar cap, this vapor undergoes photolysis to produce HO₂, which subsequently reacts with chlorine (Cl) radicals ($\text{Cl} + \text{HO}_2 \rightarrow \text{HCl} + \text{O}_2$), resulting in the formation of HCl. The sublimated water vapor and the newly produced HCl are transported to higher altitudes and toward the northern hemisphere by meridional circulation. Additionally, HCl could be locally produced by HO₂ and Cl. Based on standard photochemistry, the lifetime of HCl is expected to exceed 90 sols (Aoki et al. 2021), which cannot explain the observed nonuniform global distribution of HCl, indicating the need for a strong sink mechanism.

One possible sink is the uptake by water ice clouds, as proposed in previous studies (e.g., Aoki et al. 2021) and supported by recent observations of increased HCl in cloud-free atmospheric layers from TGO/ACS data (Luginin et al. 2024). During the southern summer, water ice cloud layers are present at high altitudes (around 50 km) over equatorial regions and lower altitudes (around 10 km) over the northern high latitudes (e.g., McCleese et al. 2010). The striking similarity in vertical profiles of water vapor and HCl observed by TGO, notably the decrease of both water vapor and HCl toward lower

altitudes at northern midlatitudes (see Figure 3(a) of Aoki et al. 2021), is consistent with the hypothesis of HCl loss through uptake by water ice clouds. Thus, the latitudinal gradient of HCl observed by iSHELL could also be attributed to the loss through uptake onto water ice particles.

Unless HCl undergoes a chemical reaction on or within the ice, converting it to another stable form of chlorine, the uptake should be a temporary sink process, since HCl is expected to be released back into the atmosphere when the ice sublimates (Aoki et al. 2021). This implies that HCl and water vapor should be controlled by the same processes, which could explain the observed strong correlation between water vapor and HCl column abundance. An irreversible or permanent sink of HCl would involve another process that is still unknown.

Given the coincidence between the appearance of HCl and the onset of the dust storm season, it is plausible that dust particles containing chlorine-bearing materials represent a source of atmospheric chlorine. Several mechanisms, involving UV irradiation of dust particles or electrostatic discharge caused by friction between particles, are potential sources of atmospheric chlorine (Aoki et al. 2021; Korabiev et al. 2021; Liuzzi et al. 2021). However, the significant correlation between HCl and water vapor might lend more support to the oxidation of dust particles (e.g., George & Abbatt 2010). The enhancement in water vapor in the southern hemisphere, along with its rise to higher altitudes during the dust storm season, where photolysis can substantially produce oxidants such as OH and HO₂, might explain the higher HCl abundances observed in the southern hemisphere.

The absence of a correlation between HCl and dust in the iSHELL data suggests that the Cl production process involving dust might be rather slow and that, once produced, HCl is controlled by processes (e.g., gas-phase chemistry and uptake onto ice particles) in which dust is not involved. However, if the oxidation of chlorides in dust particles is the dominant source mechanism, the production of oxidants by water photolysis could be a limiting factor in the production of atmospheric chlorine.





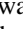
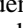
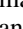

In summary, the strong correlation between HCl and water vapor observed from orbit and Earth could be explained by the

role of H₂O in various processes—namely, atmospheric chlorine production, gas-phase chemistry, and the temporary sink process involving water ice particles—that control the atmospheric evolution of HCl.

Acknowledgments

Visiting Astronomer at the Infrared Telescope Facility, which is operated by the University of Hawaii under contract 80HQTR19D0030 with the National Aeronautics and Space Administration. S.A. was supported by JSPS KAKENHI grant Nos. 22K03709, 22H05151, 22H00164, 22KK0044, and 19H00707. G.L.V. and S.F. were supported by ExoMars/TGO funds at NASA HQ and ISFM/FLaRe NASA Goddard funds. S.V. was supported by the Belgian Science Policy Office BrainBe MICROBE Project under grant No. B2/2BELB2191P1MICROBE.

ORCID iDs

S. Aoki  <https://orcid.org/0000-0001-6727-125X>
 S. Faggi  <https://orcid.org/0000-0003-0194-5615>
 G. L. Villanueva  <https://orcid.org/0000-0002-2662-5776>
 G. Liuzzi  <https://orcid.org/0000-0003-3638-5750>
 H. Sagawa  <https://orcid.org/0000-0003-2064-2863>
 F. Daerden  <https://orcid.org/0000-0001-7433-1839>
 S. Viscardy  <https://orcid.org/0000-0002-5608-7438>
 S. Koyama  <https://orcid.org/0000-0002-5944-8948>
 A. C. Vandaele  <https://orcid.org/0000-0001-8940-9301>

References

- Aoki, S., Daerden, F., Viscardy, S., et al. 2021, *GeoRL*, **48**, e92506
 Bouche, J., Coheur, P.-F., Giuranna, M., et al. 2021, *JGRE*, **126**, 2020je006480
 Daerden, F., Neary, L., Villanueva, G., et al. 2022, *JGRE*, **127**, e2021JE007079
 Gelaro, R., McCarty, W., Suárez, M. J., et al. 2017, *JCLI*, **30**, 5419
 George, I. J., & Abbatt, J. P. D. 2010, *NatCh*, **2**, 713
 Hartogh, P., Jarchow, C., Lellouch, E., et al. 2010, *A&A*, **521**, L49
 Hecht, M. H., Kounaves, S. P., Quinn, R. C., et al. 2009, *Sci*, **325**, 64
 Keller, J. M., Boynton, W. V., Karunatillake, S., et al. 2006, *JGRE*, **111**, E03S08
 Kippenberg, M., Schuster, G., Lelieveld, J., & Crowley, J. N. 2019, *ACP*, **19**, 11939
 Korablev, O., Olsen, K. S., Trokhimovskiy, A., et al. 2021, *SciA*, **7**, eabe4386
 Krasnopolsky, V. A. 2022, *Icar*, **374**, 114807
 Liuzzi, G., Villanueva, G. L., Viscardy, S., et al. 2021, *GeoRL*, **48**, e2021GL092650
 Luginin, M., Trokhimovskiy, A., & Taysum, B. 2024, *Icar*, **411**, 115960
 McCleese, D. J., Heavens, N. G., Schofield, J. T., et al. 2010, *JGRE*, **115**, E12016
 Montabone, L., Spiga, A., & Kass, D. M. 2020, *JGRE*, **125**, e2019JE006111
 Olsen, K. S., Trokhimovskiy, A., Montabone, L., et al. 2021, *A&A*, **647**, A161
 Rayner, J., Tokunaga, A., & Jaffe, D. 2022, *PASP*, **134**, 015002
 Smith, M. D. 2002, *JGRE*, **107**, 5115
 Trokhimovskiy, A., Fedorova, A. A., Olsen, K. S., et al. 2021, *A&A*, **651**, A32
 Villanueva, G. L., Mumma, M. J., & Novak, R. E. 2013, *Icar*, **223**, 11
 Villanueva, G. L., Smith, M. D., Protopapa, S., Faggi, S., & Mandell, A. M. 2018, *JQSRT*, **217**, 86
 Villanueva, G. L., Liuzzi, G., Faggi, S., et al. 2022, Fundamentals of the Planetary Spectrum Generator (NASA Goddard Space Flight Center)
 Wang, A., Jackson, A. W., Sturchio, N. C., et al. 2023, *GeoRL*, **50**, e2022GL102127